HHS Public Access

Author manuscript

Nat Methods. Author manuscript; available in PMC 2022 February 05.

Published in final edited form as:

Nat Methods. 2021 August ; 18(8): 945–952. doi:10.1038/s41592-021-01229-w.

Ultrasensitive Ultrasound Imaging of Gene Expression with Signal Unmixing

Daniel P. Sawyer[1], **Avinoam Bar-Zion**[2], **Arash Farhadi**[1], **Shirin Shivaei**[1], **Bill Ling**[2], **Audrey Lee-Gosselin**[2], **Mikhail G. Shapiro**[2,*]

[1]Biology and Bioengineering, California Institute of Technology, Pasadena, CA, United States.

[2]Chemistry and Chemical Engineering, California Institute of Technology, Pasadena, CA, United States.

Abstract

Acoustic reporter genes (ARGs) encoding air-filled gas vesicles enable ultrasound-based imaging of gene expression in genetically modified bacteria and mammalian cells, facilitating the study of cellular function in deep tissues. Despite the promise of this technology for biological research and potential clinical applications, the sensitivity with which ARG-expressing cells can be visualized is currently limited. Here we present BURST – an ARG imaging paradigm that improves the cellular detection limit by more than 1000-fold compared to conventional methods. BURST takes advantage of the unique temporal signal pattern produced by gas vesicles as they collapse under acoustic pressure above a threshold defined by the ARG. By extracting the unique pattern of this signal from total scattering, BURST boosts the sensitivity of ultrasound to image ARG-expressing cells, as demonstrated *in vitro* and *in vivo* in the mouse gastrointestinal tract and liver. Furthermore, in dilute cell suspensions, BURST imaging enables the detection of gene expression in individual bacteria and mammalian cells. The resulting capabilities expand the potential utility of ultrasound for non-invasive imaging of cellular function.

The green fluorescent protein and its analogs allow biologists to visualize gene expression and other cellular processes under an optical microscope[1]. However, the scattering of light by tissue limits the use of such optical reporter genes in intact animals[2]. In contrast, ultrasound can propagate centimeters deep into biological tissues without losing coherence, enabling the noninvasive imaging of whole organs and organisms with high spatial and temporal resolution (~100 μm and ~1 ms, respectively)[3,4]. Recently, acoustic reporter genes

---

*Correspondence should be addressed to: MGS (mikhail@caltech.edu), Phone: 626-395-8588, 1200 E. California Blvd, MC 210-41, Pasadena, CA 91125.

Author Contributions Statement

D.P.S. and M.G.S. conceived and designed the study. D.P.S., A.F., and A.B.-Z. designed the BURST pulse sequence. D.P.S. designed the BURST+ pulse sequence and the signal unmixing algorithm. D.P.S. wrote the MATLAB scripts for ultrasound imaging and data processing. A.B.-Z. prepared genetic constructs in *S. typhimurium* and *E. coli* Nissle 1917. A.F. and S.S. prepared genetic constructs in HEK cells. S.S. performed flow cytometry measurements. D.P.S. performed the *in vitro* ultrasound experiments. D.P.S., A.L.-G., and B.L. performed *in vivo* ultrasound experiments. D.P.S. and M.G.S. analyzed the data. D.P.S. and M.G.S. wrote the manuscript with input from all authors. M.G.S. supervised the research.

Competing Interests Statement

The California Institute of Technology has filed a patent application related to this article.

(ARGs) were developed for ultrasound imaging based on air-filled protein nanostructures called gas vesicles, or GVs[5]. When expressed in bacteria[6] or mammalian cells[7], ARGs allow the location and function of these cells to be monitored with ultrasound deep inside host organisms.

One of the main factors determining the utility of reporter genes is the sensitivity with which they can be detected. In previous work, ARG expression was detectable in bacteria using conventional ultrasound imaging at a concentration of 10^8 cells/ml[6]. While this density is relevant for certain *in vivo* scenarios, many applications would benefit from the ability to detect smaller numbers of cells. For example, visualizing the spatial dynamics of microbes in the intact mammalian gastrointestinal (GI) tract requires extending the sensitivity of ARG-based cellular imaging by a factor of 100–1000 while dealing with background scattering from anatomical structures[8,9,10,11,12,13]. Furthermore, in some applications, it may be necessary to detect individual genetically labeled cells. Developing such capabilities requires large improvements in sensitivity and specificity compared to existing ARG imaging techniques[14,15,6,7].

To address this need, we introduce BURST (Burst Ultrasound Reconstructed with Signal Templates) – an ultrasensitive imaging paradigm tailored to ARGs, which improves cellular imaging sensitivity by more than 1000-fold. BURST imaging exploits the strong, transient signals generated during sudden GV collapse under acoustic pressure by unmixing the temporal dynamics of such signals from background scattering. Applied to imaging engineered commensal bacteria, BURST detects cells at concentrations below 10^5 cells/ml in tissue-mimicking phantoms and visualizes cells during their passage through the mouse GI tract or uptake into the liver. Furthermore, BURST can detect ultrasound signals from individual bacteria and mammalian cells, enabling quantitative single-cell imaging. Just as the broad application of fluorescent imaging required major advances in both fluorescent proteins and optical detection methods, the development of BURST imaging complements recent advances in ARGs to broaden the potential applications of biomolecular ultrasound.

Results

The BURST method: selective imaging of ARG-expressing cells

BURST creates GV-specific ultrasound images by exploiting the phenomenon of GV collapse. GVs comprise a 2 nm-thick protein shell enclosing a hollow, air-filled compartment with dimensions on the order of 200 nm[16,17] (Fig. 1a). GVs self-assemble inside cells from the constituent proteins encoded in ARGs[6,7]. When these nanostructures are exposed to pressures above their genetically defined collapse threshold, their shell breaks (Fig. 1a) and their air contents are rapidly dissolved into the surrounding media. The collapse of GVs under acoustic pressure generates a strong transient ultrasound signal[7,18]. In BURST imaging, we rapidly acquire a series of ultrasound images during which the transmit pressure undergoes a step-change from a value below the GV collapse threshold to above it (Fig. 1b). This step-change generates a transient collapse-based signal increase in voxels containing GVs, while the signal from non-GV linear scatterers steps up and persists with the higher applied pressure (Fig. 1b). The images acquired during this pulse train combine to form a time-series vector for each voxel in the field of view (Fig. 1

c–d). In BURST signal processing, we decompose these vectors into weighted sums of template vectors representing the expected signal patterns of GVs, linear scatterers and background noise or offset, allowing us to generate images specific to each source of signal (Fig. 1e). We hypothesized that by effectively isolating the strong signal impulse generated by GVs at the moment of their collapse, while subtracting background linear contrast, BURST imaging would substantially improve the detection sensitivity of GV-expressing cells. Importantly, GV collapse is well-tolerated by both bacterial and mammalian cells, which can subsequently re-express new GVs to allow additional imaging[6,7].

Temporal modulation of contrast agent signals has been used to enhance the detection of synthetic ultrasound contrast agents such as microbubbles[19] and nanodroplets[20], and has formed the basis for improved sensitivity and resolution in photoacoustic imaging[21,22] and fluorescence microscopy[23]. Likewise, destruction of contrast agents via high-pressure ultrasound pulses has been used to increase contrast in both ultrasound and photoacoustic imaging[24–27], often coupled with therapeutic applications[26,27]. However, each class of reporters requires a unique approach based on their physical properties. For example, while individual microbubbles are detectable in many contexts as single sources using nondestructive pulse sequences, GVs and ARG-expressing cells are not. It is therefore critical to develop and optimize a method such as BURST, which is tailored to maximizing the detection sensitivity of ARGs based on their unique, nonlinear acoustic properties.

To test the BURST protocol, we prepared gel phantoms containing pairs of rectangular wells filled with either ARG-expressing *E. coli* Nissle cells or red fluorescent protein (RFP)-expressing controls (Fig. 2a). The cells were embedded in an agarose-based tissue-mimicking material (TMM)[28] with strong linear scatterers providing background contrast. For initial experiments, we used bacteria at a concentrations of 10^7 cells/ml, which is 10-fold lower than the previously published *in vitro* detection limit[6]. In the initial low-pressure image frame acquired with 0.27 MPa peak positive pressure (PPP), little signal was observed in either well (Fig. 2b). In the second frame, acquired at the stepped-up pressure of 4.3 MPa, both samples showed substantial signal, with the signal from ARG-expressing cells enhanced by 9 dB relative to that from RFP controls. By the next frame, this signal difference disappeared, as expected with GV collapse, leaving behind the linear scattering from the TMM.

Using the BURST algorithm, we decomposed the temporal signal vector in each well (Fig. 2c) into its contributions from GVs, linear scatterers and noise (Fig. 2d). Performing this operation for each pixel in our field of view, we obtained images corresponding to each signal type (Fig. 2 e–f). The image corresponding to GV-specific signal shows clear contrast between the well containing ARG-expressing cells and the control well, with a contrast-to-tissue ratio (CTR) of 32 dB (Fig. 2e). Background scattering is not visible in this image due to thresholding of the color scale (Extended Data Fig. 1). Meanwhile, the image corresponding to the linear scattering component showed a similar level of signal in each well (Fig. 2f).

In addition to our basic BURST paradigm, which uses a single-cycle transmit waveform (Fig. 2g), we hypothesized that we could further boost detection sensitivity by extending

the transmit waveform to multiple cycles. This hypothesis is based on the fact that following GV collapse, the air contained inside GVs is liberated as free nanobubbles, which can be cavitated with extended pulses[18]. To test this possibility, we extended the transmitted waveform to 3 cycles, naming the resulting imaging mode BURST+ (Fig. 2h). As hypothesized, ARG-expressing Nissle cells (at 10^7 cells/ml) imaged with BURST+ showed a signal enhancement of 6 dB relative to BURST. Detailed acoustic measurements confirmed that the BURST+ signal is predominantly generated by sustained stable cavitation of liberated nanobubbles, while BURST signal is generated by more transient dynamics (Extended Data Fig. 2). Both pulse types resulted in the complete collapse of GVs inside imaged bacteria (Extended Data Fig. 3). The frequency, pressure level and pulse duration used in BURST and BURST+ imaging are not expected to result in spontaneous cavitation in tissues[29]. The acoustic pressure required to generate BURST signal depends on the type of GV being imaged (Extended Data Fig. 4).

In vitro detection limit for BURST imaging

To determine the cellular detection limits for BURST and BURST+, we imaged tissue-mimicking agarose phantoms containing ARG-expressing and RFP-expressing *E. coli* Nissle cells at concentrations ranging from 10^3 cells/ml to 10^8 cells/ml. In conventional B-mode images, it was challenging to make out clear GV contrast at any cell concentration (Fig. 3a). However, BURST images showed clear GV contrast down to 10^5 cells/ml (Fig. 3b), while BURST+ images showed clear GV contrast down to 10^4 cells/ml (Fig. 3c). This represents improvements of 1000-fold and 10,000-fold, respectively, over the previously reported detection limit[6]. Quantification across multiple replicates (Fig. 3d) confirms these detection thresholds with a mean CTR greater than 6 dB. BURST and BURST+ signals increased with cell concentration up to approximately 10^6 cells/ml and thereafter plateaued, likely due to acoustic shielding (Extended Data Fig. 5).

While these experiments used TMM phantoms to identify detection limits relevant for *in vivo* imaging, in less echogenic tissues or blood vessels, the cells may be surrounded by a low-scattering medium. In agarose phantoms mimicking such conditions, the unmixed signals from ARG-expressing cells were reliably detectable at cell concentrations down to 10^3 cells/ml (Extended Data Fig. 6).

BURST imaging of bacterial passage in the small intestine

Having demonstrated the ability of BURST imaging to provide sensitive imaging of bacterial gene expression *in vitro*, we set out to test the ability of this method to visualize cells in a living animal. Bacteria play major roles in the mammalian microbiome, influencing everything from metabolism and immunity to neurological function[8,9,10,11,12,13]. In addition, many synthetic biology efforts are focused on engineering bacterial cells as diagnostic or therapeutic agents in the GI tract[13]. Previously, ARG-expressing *E. coli* were imaged in the mouse colon after direct rectal injection in agarose phantoms containing 10^9 cells/ml[6]. However, imaging living cells in the more complex environment of the small intestine during their passage through this GI segment was not demonstrated.

To evaluate the ability of BURST to image cells *in vivo* following oral administration, we gavaged wild-type mice with an attenuated strain of *Salmonella typhimurium* engineered to express ARGs, or with control cells expressing the luminescent LUX operon[6] (Fig. 4a). Two hours later, we acquired BURST images at multiple transverse planes covering the abdominal cavity of each mouse. Display images were generated by overlaying grayscale B-mode images with heatmaps representing the GV-specific BURST signal (Fig. 4 b–e). In all but one mouse gavaged with ARG-expressing cells, we observed contiguous patches of supra-threshold BURST signal (Fig. 4b). The anatomical region containing this signal corresponds to the expected location of the small intestine[30]. We did not observe a similar BURST signal in the abdomen of control mice gavaged with LUX-expressing cells (Fig. 4c). Aggregating the mean BURST CTR in the upper abdominal cavity in each image plane across mice shows a consistent signal in the ARG-expressing group for all image planes spanning 16 mm to 22 mm below the rib cage (Fig. 4f). These results validate the ability of BURST imaging to reliably visualize ARG expression in live cells passing through the mouse GI tract.

BURST imaging of bacterial entry into liver from circulation

Having established the ability of BURST to image ARG-expressing bacteria in the GI tract, we set out to test the ability of this method to image an *in vivo* biological process with faster dynamics and lower cellular concentrations. In particular, we examined the problem of organ biodistribution for systemically administered bacterial agents. This is an important problem in the field of engineered probiotics[13], which are designed to home to specific organs upon intravenous injection but are often administered at too low a concentration to image until several days later, when the cells proliferate in target tissues. We hypothesized that the sensitivity of BURST would allow us to monitor the entry of systemically injected bacteria into a specific tissue in real time.

To test this hypothesis, we injected 50 μl of ARG-expressing *S. typhimurium* at 3×10^5 cells/ml into the tail veins of mice and used BURST+ to image the uptake of the cells into the liver (Fig. 5a), a key organ targeted[31] by this probiotic chassis[32]. Following an initial BURST+ acquisition used to validate the positioning of the probe, we acquired a pair of BURST+ images every minute to visualize cells accumulated in the liver as well as those passing through the liver vasculature. The first image in this pair was acquired 50 s after the previous set (Fig. 5b), while the second image was taken 10 s later (Fig. 5c). The 50 s image contains a combination of signal from cells taken up by the liver over the preceding 50 s and any cells inside the liver vasculature at that moment. The acquisition taken 10 s later contains a greater proportion of signal coming from cells passing through the vasculature, which is replenished more quickly by blood flow compared to the slower process of liver uptake. We repeated these acquisitions every minute until no appreciable BURST+ signal was discernable by eye. As a control, we performed the same procedure using cells whose GVs were hydrostatically pre-collapsed prior to injection (Fig. 5 d–e).

We observed robust BURST+ signal in the livers of mice injected with ARG-expressing cells that steadily decreased over time and became indistinguishable from background after 25 min (Fig. 5 f–g). A similar signal was not seen in mice injected with pre-collapsed cells.

Since BURST acquisition erases the signal from ARG-expressing cells, each successive image represents new cells that have entered the tissue, corresponding to a differential of cumulative uptake. To estimate accumulation, we integrated the 50 s signals above baseline over time, after first subtracting from each time point its paired 10 s signal to remove the approximate vascular contribution. The resulting estimate suggests that ARG-expressing cells continue to accumulate in the liver for 20 min following injection (Fig. 5h).

Notably, the punctate BURST+ signal observed in the early 10 s acquisitions (Fig. 5c) closely resembled, in shape and intensity, the BURST+ images of 10^3 cells/ml ARG-expressing cells embedded in clean agarose (Extended Data Fig. 6c). Accounting for our injected cell concentration, typical mouse blood volume of 1.5 ml and blood volume fraction in the mouse liver of 36% [33], we expect the liver in these recirculation images to contain no more than 3.6×10^3 cells/ml. Moreover, considering the clearance of bacterial cells from the bloodstream, it is reasonable to expect cell concentrations below 10^3 cells/ml at later time points, in which case fewer than ~15 cells would be expected to be present in the volume captured by our effective field of view. While it is impossible in the present study to directly confirm single-cell detection *in vivo,* the range of expected concentrations and the punctate nature of the observed signals would be consistent with this possibility.

These results demonstrate that BURST can noninvasively image genetically labeled cells in the context of a dynamic biological process in living animals at ultra-low concentrations. In addition, we did not note any obvious adverse effects in the mice following this experiment.

BURST+ imaging enables single-cell detection

The observation of punctate signals in BURST+ images at cell densities of $10^3 – 10^4$ cells/ml (Fig. 3c, Fig. 5b–c, and Extended Data Fig. 6) suggested that this imaging method may be capable of detecting signals from individual ARG-expressing cells. To test this hypothesis, we used BURST+ to image dilute samples of ARG-expressing and RFP-expressing Nissle cells, suspending them in degassed phosphate-buffered saline (PBS) at concentrations below 500 cells/ml (Fig. 6a). BURST+ images of ARG-expressing cells showed clear punctate signals, the number of which increased with the cell concentration (Fig. 6b). In contrast, RFP-expressing controls rarely showed any such signals (Fig. 6c). In suspensions of ARG-expressing cells, the number of distinct sources increased linearly with cell concentration (R=0.86) and closely matched the number of cells expected from optical counting (Fig. 6d). In contrast, RFP-expressing controls had few signals and no significant dependence on cell concentration (R=0.08, p=0.32, linear correlation).

Following the single-cell imaging of bacterial cells, we tested the ability of BURST+ to detect GV expression in individual mammalian cells, which are larger than bacteria but have lower GV expression levels[7]. We imaged suspensions of HEK cells genetically engineered to express either mammalian acoustic reporter genes (mARGs), or the control fluorophore mCherry. Punctate signal sources could clearly be seen in BURST+ images of suspended mARG-expressing cells, with the number of such sources increasing linearly with cell concentration (R=0.79) (Fig. 6e). Similar sources were rarely seen with mCherry control cells (Fig. 6f), and their number did not correlate with cell concentration (R=0.07, p=0.39, linear correlation) (Fig. 6g). The number of ultrasound sources counted for

mARG-expressing cells constituted only about half the number of cells expected based on optical counting. We suspect that this discrepancy arose from the heterogeneity of gene expression in this cell line (in which, unlike the bacterial samples, we cannot pre-select cells for imaging based on ascertained GV expression). Nevertheless, the fact that the number of punctate signals was of the expected order of magnitude and scaled linearly with concentration demonstrates that BURST+ detects single-cell signals from both ARG expressing bacteria and mammalian cells.

BURST imaging preserves cell viability

To assess the cytocompatibility of BURST imaging, we quantified the viability of bacterial and mammalian cells and the ability of bacterial colonies to re-express GVs after exposure to this imaging mode. We found no significant impact on bacterial colony growth or re-expression ($p=0.1$, two-sided two-sample t-test), a small reduction in individual bacterial cell viability, and no significant impact on the viability of mammalian cells (BURST: $p=0.83$, BURST+: $p=0.48$, exact permutation test) (Extended Data Figs. 7–8).

Discussion

Taken together, the results of this study demonstrate the ability of the BURST imaging paradigm to provide ultrasensitive ultrasound imaging of gene expression with an improvement of more than 1000-fold compared to the state of the art. BURST achieves this unprecedented sensitivity by taking advantage of the unique temporal signal generated by monodisperse populations of collapsing GVs, unmixed from both surrounding and co-localized scatterers using a simple linear algorithm. This advance complements rapidly progressing efforts to develop and apply ARGs and GVs to a broad range of biological applications[4,6,7,18, 35,36,37] and will enable the imaging of these acoustic biomolecules with increased sensitivity and specificity without changes to their composition. Moreover, we expect the sensitivity of BURST to lower the barrier for initial applications of ARG-based imaging in challenging settings by facilitating the detection of low ARG expression levels or small ARG-labeled cell densities. While BURST imaging requires the collapse of GVs, their subsequent re-expression as a genetically encoded reporter, taking place on the timescale of hours to days[6,7], should enable the imaging of a variety of dynamic processes with kinetics beyond this timeframe.

Future improvements would help BURST imaging achieve widespread use. For example, to enable rapid BURST imaging over a large field of view, it would be helpful to develop ultrasound imaging transducers capable of higher transmit pressures. Alternatively, the pressure requirement could be reduced by engineering ARGs to encode GVs with lower critical collapse pressures. Indeed, whereas the acoustic collapse mid-point of the ARGs used in this study is 2.7 MPa[6], certain engineered GVs collapse at pressures below 0.6 MPa[35], and purified GVs from different species produce BURST signals at different pressure thresholds. Lower pressure would also be expected to mitigate the already-minor effects of BURST imaging on cell viability, which itself should be extended to investigate other potential cellular side-effects in specific application scenarios.

The engineering of fluorescent proteins with improved and modified properties, such as selective photoactivation[1,38], went hand-in-hand with complementary innovations in microscopy and image processing, such as PALM[39], STORM[40], and light sheet microscopy[41], resulting in ever-improving resolution, scale, and information content. We envision a similar synergy in the evolution of acoustic proteins and ultrasound imaging techniques.

Methods

The research methods employed in this study comply with all relevant ethical regulations. Animal experiments were approved by the Institutional Animal Care and Use Committee of the California Institute of Technology.

Bacterial expression

Plasmids encoding ARGs were transformed into chemically competent *E. coli* Nissle 1917 (Ardeypharm GmbH) and grown in 5 ml starter cultures in LB medium with 50 μg/ml kanamycin, 2% glucose for 16 h at 37 °C. Large-scale cultures in LB medium containing 50 μg/ml kanamycin and 0.2% glucose were inoculated at a ratio of 1:100 with the starter culture. Cells were grown at 37 °C to OD600nm = 0.3, then induced with 3 μM IPTG. Cells were cultured for 22 h at 30 °C, then centrifugated for 4 hours at 150 x g and 4 °C to enrich for buoyant cells. Cells in the buoyant fraction were used for experiments involving agarose phantoms. Neutrally buoyant cells in the supernatant below the buoyant fraction were used for all other experiments involving ARG-expressing Nissle cells. The same expression protocol was followed to produce mRFP-expressing Nissle cells, except that cells were resuspended from the pellet in PBS following centrifugation.

GV-expressing *Salmonella typhimurium* of the attenuated, tumor-homing strain ELH1301[42] were produced by transforming cells with a plasmid encoding an engineered genetic construct comprising either a GV operon or, as a control, a NanoLuc luciferase. Constructs were assembled using Gibson cloning. The genetic constructs were cloned into the pTD103 plasmid (gift from J. Hasty, University of California, San Diego), with expression driven by a luxI promoter upon induction with 3nM N-(β-ketocaproyl)-l- homoserine lactone (AHL). The cells were cultured for 24 hours at 30 °C after induction, then centrifugated for 4 hours at 150 x g and 4 °C to enrich for buoyant cells. Cells in the buoyant fraction were used for *in vivo* experiments.

In experiments employing multiple bacterial biological replicates, replicates correspond to cells cultured from separate colonies from the same transformation.

Mammalian cell expression

mARG-expressing and mCherry-expressing HEK cells were previously described[7]. Briefly, HEK293tetON cells were genetically engineered with mARG gene cassettes (Addgene 134343, 134344 and 134345) using the piggyBac transposase system and a monoclonal culture was created by flow cytometry (BD FACSAria III). Similarly, mCherry-expressing cells were created by genetically engineering HEK293tetON cells with mCherry using the piggyBac transposase system. Cell cultures were maintained in DMEM supplemented with

10% tetracycline-free FBS (Clontech) and penicillin and streptomycin. For BURST imaging, both types of cells were seeded in 10 cm plates, and once they reached 70–80% confluency treated with 1 μg/mL doxycycline and 5 mM sodium butyrate for 72 hours. Cells were then trypsinized and resuspended in media before being stained 1:1 with Trypan blue dye and counted using a disposable hemocytometer (C-chip DHC S02, Incyto) under a brightfield microscope.

Ultrasound pulse sequence and data acquisition

Ultrasound imaging for all experiments was performed using a Verasonics Vantage programmable ultrasound scanning system. *In vitro* experiments were done using an L10–4v 128-element linear array transducer (Verasonics). Image acquisition was performed using a custom imaging script with a 64-ray-lines protocol with a synthetic aperture of 65 elements to form a focused excitation beam. The programmable transmit focus was set to 20 mm to be aligned with the fixed elevation focus of the transducer. The transmit waveform was set to a frequency of 6 MHz, 67% intra-pulse duty cycle resulting in sinusoidal pulses. BURST pulse sequences consisted of a single low-pressure frame (transducer voltage = 1.6 V, peak positive pressure = 0.27 MPa) followed by five high-pressure frames (transducer voltage = 50 V, peak positive pressure = 4.3 MPa). The frame rate was 111 Hz. A similar imaging sequence was used for the *in vivo* experiments, with some modifications detailed below in the relevant section.

BURST processing algorithm

BURST images are generated by applying a temporal template unmixing algorithm across individual pixel locations in the frame stack. The input to the algorithm at the single pixel level consists of a 6-element vector, corresponding to pixel values in each frame. The parameters of the algorithm are the following template vectors for GVs ($u_g = \left[0\ 1\ 0\ 0\ 0\ 0\right]^T$), linear scatterers ($u_s = \left[0\ 1\ 1\ 1\ 1\ 1\right]^T$) and offset ($u_o = \left[1\ 1\ 1\ 1\ 1\ 1\right]^T$).

The template unmixing model is represented by the linear equation $Uw = p$, where the template vectors are concatenated into the template matrix $U = \left[u_s\ u_o\ u_g\right]$, and w contains the weights for each template. For each pixel vector p, least squares solution for the template weights is obtained by the pseudoinverse:

$$w = \left(U^T U\right)^{-1} U^T p$$

The w_g component of $w = \left[w_s\ w_o\ w_g\right]$ was selected as the output of the algorithm. More generally, U can be an $n \times m$ matrix, where n is the length of p and the number of image frames and m is the length of w and the number of signal templates.

In theory, because negative weights have no meaning in this model, a proper estimation of the template weights would require the appropriate constrained linear least squares solution, which is typically two orders of magnitude slower to compute. However, it was found empirically that setting all negative values of the unconstrained solution to zero results

in a final image that is not appreciably different from that obtained using the constrained solution. The template unmixing algorithm was applied offline to acquired BURST data. All image processing was implemented in MATLAB (version 9.5.0.1298439).

In vitro phantom imaging

Phantoms for imaging were prepared by melting 1% (w/v) agarose in PBS and casting wells using a custom 3D-printed template with 48 wells with dimensions of 6 mm × 5 mm × 2 mm. ARG- and RFP-expressing Nissle cells (at 2× the final concentration and at 25 °C) were mixed in a 1:1 ratio with molten agarose or molten TMM (at 2× the final concentration and at 56 °C) and immediately loaded into the phantom. The concentration of cells was determined before diluting and loading by measuring their OD_{600nm}. TMM consisted of 1% (w/v) agarose, 0.53% (w/v) 37 μm silicon carbide, 0.94% (w/v) 3 μm aluminum oxide, 0.88% (w/v) 0.3 μm aluminum oxide, and 96.65% (w/v) PBS, similar to the TMM described by Ramnarine *et al.* (2001)[28] but with lower agarose content and no glycerol or antibiotic. Special care was taken to thoroughly degas the molten agarose to reduce the number of microbubbles present in the gel. The phantoms were imaged at 6 MHz, using a single-cycle transmit waveform to maximize axial resolution. Parabolically focused B-mode pulses were used to achieve the PPP needed for GV collapse. Frames were acquired every 9 ms to minimize any impact from motion.

In vivo imaging of gavaged cells

All *in vivo* gavage experiments were performed on female BALB/cJ mice under a protocol approved by the Institutional Animal Care and Use Committee of the California Institute of Technology. Animal housing room temperatures were monitored at all times and maintained between 71 and 75 °F. Humidity was maintained between 30–70%. Automated light timers ensured a consistent light-dark cycle with 13 hours on and 11 hours off. No randomization or blinding were necessary in this study. Mice were anesthetized with 1–2% isoflurane, maintained at 37 °C on a heating pad, depilated over the imaged region, and imaged using an L11–4v transducer attached to a manipulator. For imaging of gavaged *Salmonella typhimurium* in the gastrointestinal tract, mice were placed in a supine position, with the ultrasound transducer positioned over the upper abdomen such that the transmit focus of 12 mm was close to the top of the abdominal wall. Two hours prior to imaging, mice were gavaged with 200 μl of buoyancy-enriched *Salmonella typhimurium* at a concentration of 10^9 cells/ml. No fasting, bicarbonate administration, or other pretreatments were used.

To mitigate tissue motion during *in vivo* imaging, a rapid BURST script was implemented that transmits and acquires three 32-aperture focused beams at a time, improving the frame rate by a factor of 3 to 333 Hz. To maximize spatial resolution, the transmit waveform was set to a frequency of 11.4 MHz. The transmit focus was set at 12 mm to match the expected location of the small intestine relative to the transducer, which had to be positioned in relatively close proximity to maintain acoustic coupling.

Prior to processing with template unmixing, a 2 × 2 median filter followed by a gaussian blur filter with $\sigma = 1$ was applied to each 2D image frame of each image plane of each mouse. The images output from template unmixing were then concatenated into a 3D array

to which a 1 × 1 × 3 median filter was applied to remove isolated motion artifacts. The resulting 2D BURST images were then dB-scaled and overlaid on the square-root-scaled B-mode image representing frame 1 in the corresponding timeseries. The BURST images were overlaid in locations where the BURST image pixel values exceeded a threshold of 105 dB, which was chosen as the minimum threshold at which no residual motion artifacts were visible in the dorsal half of the abdominal cavity, where no BURST signal was expected. BURST images were pseudo-colored with the hot colormap and B-mode images with the gray colormap. Quantification was performed by manually drawing an ROI covering the ventral half of the abdominal cavity in each image plane for each mouse.

In vivo imaging of intravenously injected cells

All *in vivo* IV imaging experiments were performed on female BALB/cJ mice aged 16 weeks under a protocol approved by the Institutional Animal Care and Use Committee of the California Institute of Technology. No randomization or blinding were necessary in this study. Mice were anesthetized with 1–2% isoflurane, maintained at 37 °C on a heating pad, depilated over the imaged region, and imaged using an L10–4v transducer attached to a manipulator. The same BURST+ pulse sequence used in *in vitro* experiments, rather than the modified pulse sequence used for gavage imaging, was used for this experiment since tissue motion due to peristalsis was not a concern. Mice were placed in a supine position, with the ultrasound transducer positioned such that the transmit focus of 15 mm was at the center of the liver. Following insertion of a catheter with a 30 g needle into the lateral tail vein, mice were injected with 50 μl of buoyancy-enriched ARG-expressing *S. typhimurium* at a concentration of 3×10^5 cells/ml in PBS.

After allowing injected cells to circulate for one minute, one or more BURST+ images were acquired during a survey period in which the probe was repositioned along the rostral-caudal axis until the appearance of a large signal indicated the correct location. Following the survey period, which lasted one to nine minutes, two BURST+ images were acquired each minute in alternating intervals of 50 s and 10 s until signal in the liver was not distinguishable from background. After all BURST+ images were acquired, an anatomical B-mode image was acquired using the WideBeamHISC script provided with the Verasonics software.

Prior to processing with template unmixing, a 2 × 2 median filter was applied to each 2D image frame. BURST images were pseudo-colored with the hot colormap and B-mode images with the gray colormap. Quantification was performed by manually drawing an ROI around the liver and computing the mean BURST+ signal. We extracted two time series from the quantifications from each mouse: one for the 50 s intervals and one for the 10 s intervals, each indexed by time since injection. To obtain mean signal curves, locally weighted scatterplot smoothing with quadratic regression and a 15% span was applied separately to each of these time series. For each time series, linear interpolation was then applied with query points consisting of the set of all unique time points across all the time series that fell between the first and last time points of the interpolant.

Single-source counting

Cells were suspended in liquid buffer to allow thorough degassing of the medium to eliminate most microscopic air bubbles, which could otherwise act as confounding sources of signal.

Hydrophone measurements of the ultrasound transducer's acoustic field were used to estimate the out-of-plane dimension of the 3D (FOV) in which ARG-expressing cells are expected to experience collapse dependent signal (2 mm). The out-of-plane FOV boundaries were defined as the displacement at which the peak positive acoustic pressure is equal to the acoustic collapse mid-point of the *E. coli*-expressed ARGs used in this study[6]. These measurements were performed using a fiber-optic hydrophone system with a tapered sensor tip (Precision Acoustics) immersed in a tank filled with water that had been conditioned overnight using an AQUAS-10 water conditioner (Onda). The lateral dimension of the FOV (19.5 mm) was determined by the number of ray lines used to form the ultrasound image. The axial dimension (1 mm) was set by restricting the axial region of the BURST images displayed for counting to this size, which was chosen to cover the region around the transducer focus over which the mean BURST signal intensity was relatively constant. Based on these hydrophone measurements of the beam profile of BURST+ transmit pulses, it was estimated that cells in a 1 mm × 19.5 mm × 2 mm field of view (FOV) would experience sufficient pressure to generate collapse-dependent signal.

Prior to counting, cells were diluted to an estimated 10^6 cells/ml and were then incubated at 25 °C for 30 min with BacLight Green fluorescent dye (Invitrogen). 10 μl of the cell suspension was loaded onto a C-Chip hemocytometer (SKC, Inc.) and cells were counted at 10x magnification with an Observer.A1 microscope (Zeiss). Estimates of the expected ground truth number of cells per image for each cell concentration were obtained by combining this optical cell count data with the FOV volume estimate obtained through hydrophone measurements.

For validation of single-cell detection, the L10–4v transducer was mounted on a BiSlide computer-controlled 3D translatable stage (Velmex) above a 4 L container containing 3.8 L water that had been circulated through the water conditioner for 1 hour. 200 ml of 20x PBS was then gently added to the water, with the mouth of the PBS-containing bottle at the level of the surface of the water to avoid creating bubbles. A piece of acoustic absorber material was placed at the bottom of the bucket to reduce reflections. A MATLAB script was written to control the Verasonics system in tandem with the BiSlide stage, which was programmed to move 1 cm after each BURST+ acquisition. After each set of BURST+ acquisitions (starting with plain PBS), 30 μl of 10^6 cells/ml ARG-expressing Nissle cell suspension was added to the bucket, which was gently stirred with a glass rod. A separate bucket with freshly conditioned water and buffer was used for the RFP control cells.

We wrote a MATLAB script to display a 1 mm × 19.5 mm segment, centered at the point of highest average intensity, of all BURST images (all replicates, all concentrations, and RFP vs. ARG cells) in a random order, blinding the experimenter to the condition when performing source counting.

Collapse signal characterization

Collapse signal characterization experiments were performed with the same liquid buffer suspension setup and protocol used for single-source validation, apart from the variations in sequence parameters described in Extended Data Fig. 2.

To capture the sub-millisecond dissolution times of the nanobubbles, an ultrafast version of the BURST+ pulse sequence was implemented in which the full timeseries of low- and high-pressure acquisitions is done for each ray line, rather than for each frame. This results in a significantly shorter delay between frames for any given location in the image at the expense of significantly longer delays between separate ray lines.

Bacterial colony growth assay

ARG Nissle cells were transformed as described above. The transformation mix after recovery was plated on a 4-layer LB-Agar plate. In addition to LB and 50 μg/ml kanamycin, the first (bottom) layer contained 1% agarose and 7.5 μM IPTG; the second layer 1% agarose and 1% glucose; and the third layer 0.25% agarose, 1% glucose, and 10 cells/ml of the transformed Nissle. The fourth (top) layer contained 0.25% agarose in PBS with 1% glucose and 50 μg/ml kanamycin. The first and second layers were 4 mm thick and the third and fourth layers were 1 mm thick.

After culturing for 15 h at 30 °C, a darkfield optical image of the plate was acquired using a gel imager (BioRad). The plate was then immersed in PBS to allow acoustic coupling to the L10–4v transducer. The transducer was connected to the BiSlide motor stage and aligned perpendicular to the plane of the plate at a distance of 20 mm from the LB-Agar layer containing the ARG-expressing colonies. One half of the plate was exposed to BURST+ by applying the sequence to planes spaced by 1 mm across the plate. The plate was incubated for an additional 23 h at 30 °C.

A second darkfield optical image of the plate was acquired following the second round of incubation. The BURST+ plate scan was then repeated to obtain images confirming GV re-expression.

Bacterial colony-forming assay

Neutrally buoyant ARG Nissle cells were exposed to ultrasound inside cylindrical inclusions in agarose gel in 3D-printed acoustic cuvettes with windows covered by mylar. Each cuvette was filled with molten 1% agarose gel and a 3D-printed cylindrical plug was used to cast a cylindrical inclusion with 40 mm length and 2 mm diameter. Each ARG Nissle sample was diluted to 10^5 cells/ml in PBS. 50 μL of the resulting suspension was loaded into the inclusion in the acoustic cuvette, which was placed in a water tank. The L10–4v transducer was attached to an XSlide translatable motor stage (Velmex), submerged in a water tank, and aligned such that the 20 mm transducer focus was positioned at the center of the inclusion. A single pulse sequence was applied to each sample, using either BURST+, BURST, or, in the control case, B-mode with 3 cycles and a PPP of 0.3 MPa. 20 μL of sample was then extracted from the inclusion and diluted with PBS to 10^4 cells/ml. 100 μL of this dilution

was plated on Lennox LB agar with 50 μg/ml kanamycin and 2% glucose. Plates were incubated for 20 hours at 30 °C.

Cell viability was measured by counting the number of colonies formed from samples exposed to BURST or BURST+ and dividing by the number of colonies formed from the same biological replicate exposed to the control condition.

Mammalian cell viability assay

HEK cells from an mARG-expressing cell line were trypsinized and pelleted by centrifugation at 400 g for 4 min at 4 °C. The pelleted cells were then resuspended in PBS and diluted to a concentration of 2.5×10^5 cells/ml. These samples were then exposed to ultrasound and collected with the same protocol used for ARG-expressing bacteria described above.

After ultrasound exposure, cells were stained with Zombie NIR viability dye (BioLegend Inc.) following the manufacturer's protocol. Relative cell death was measured using the Beckman Coutler Cytoflex Flow Cytometer (Beckman Coutler Inc.) based on Zombie NIR fluorescence. This assay was validated with a positive control condition in which HEK cells were incubated at 80 °C for 1 minute, resulting in 100% measured cell death. The gating strategy is shown in Supplementary Fig. 1.

BURST threshold imaging

The BURST experiments were performed with the same liquid buffer suspension setup used for single-source validation. The pulse sequence was modified such that only one out of every twelve ray lines were transmitted. This was done to avoid collecting data from GVs collapsed by the periphery of the beams transmitted along adjacent ray lines.

Halo GVs were purified from *Halobacterium salinarium*, Ana GVs were purified from *Anabaena flos-aquae*, and Mega GVs were purified from *E. coli* using the protocols described in Lakshmanan *et al.* (2017)[43], with Mega GVs unclustered using urea. All GV samples were diluted to 10^{-5} optical density at 500 nm (OD_{500}). After taking the mean of each ray line, the data was converted to dB scale and then normalized to facilitate comparison of thresholds.

TEM sample preparation and imaging

Cells expressing ARGs were placed into 10 mM HEPES pH 8.0 following exposure to ultrasound with the same protocol described above for the bacteria cell viability experiments, except that the agarose was cast with 10 mM HEPES pH 8.0 instead of PBS. Samples were deposited on Formvar-carbon 200 mesh grids (Ted Pella) that were rendered hydrophilic by glow discharging (Emitek K100X). 2% uranyl acetate was added for staining. The samples were then imaged on a FEI Tecnai T12 transmission electron microscope equipped with a Gatan Ultrascan CCD.

Software

MATLAB (version 9.5.0.1298439, Mathworks) was used for collapse measurements, and MATLAB custom scripts, with functions provided as part of the Vantage (version 4.0.0, Verasonics) software, were used to acquire and process ultrasound images. Optical Density of samples was measured using the NanoDrop 2000c software (version 1.5, Thermo Fisher Scientific). FloJo (version 10.6.1) was used to process flow cytometry data. Figures were composed using Adobe Illustrator CS6 (version 16.0.4, Adobe) and Affinity Designer (version 1.8.3, Serif Europe).

Code availability

MATLAB code is available via GitHub (https://github.com/shapiro-lab/burst-imaging-public).

Data availability

Statistical source data is provided in Supplementary Information. Primary image data is available via GitHub (https://github.com/shapiro-lab/burst-imaging-public).

Extended Data

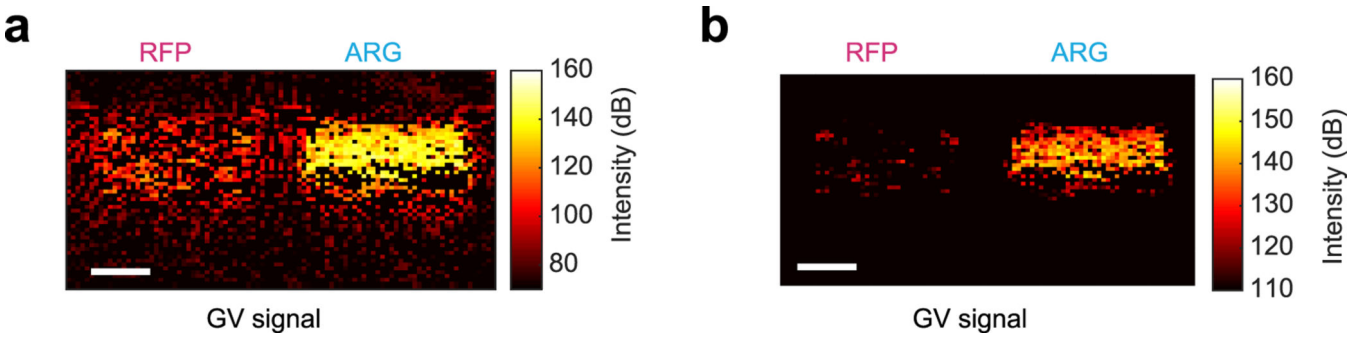

Extended Data Fig. 1. BURST background signal in phantoms

(**a**) The same image data from Fig. 2e displayed with a lower limit of 70 dB on color scale. (**b**) Fig. 2e, shown for comparison. All scalebars: 2 mm.

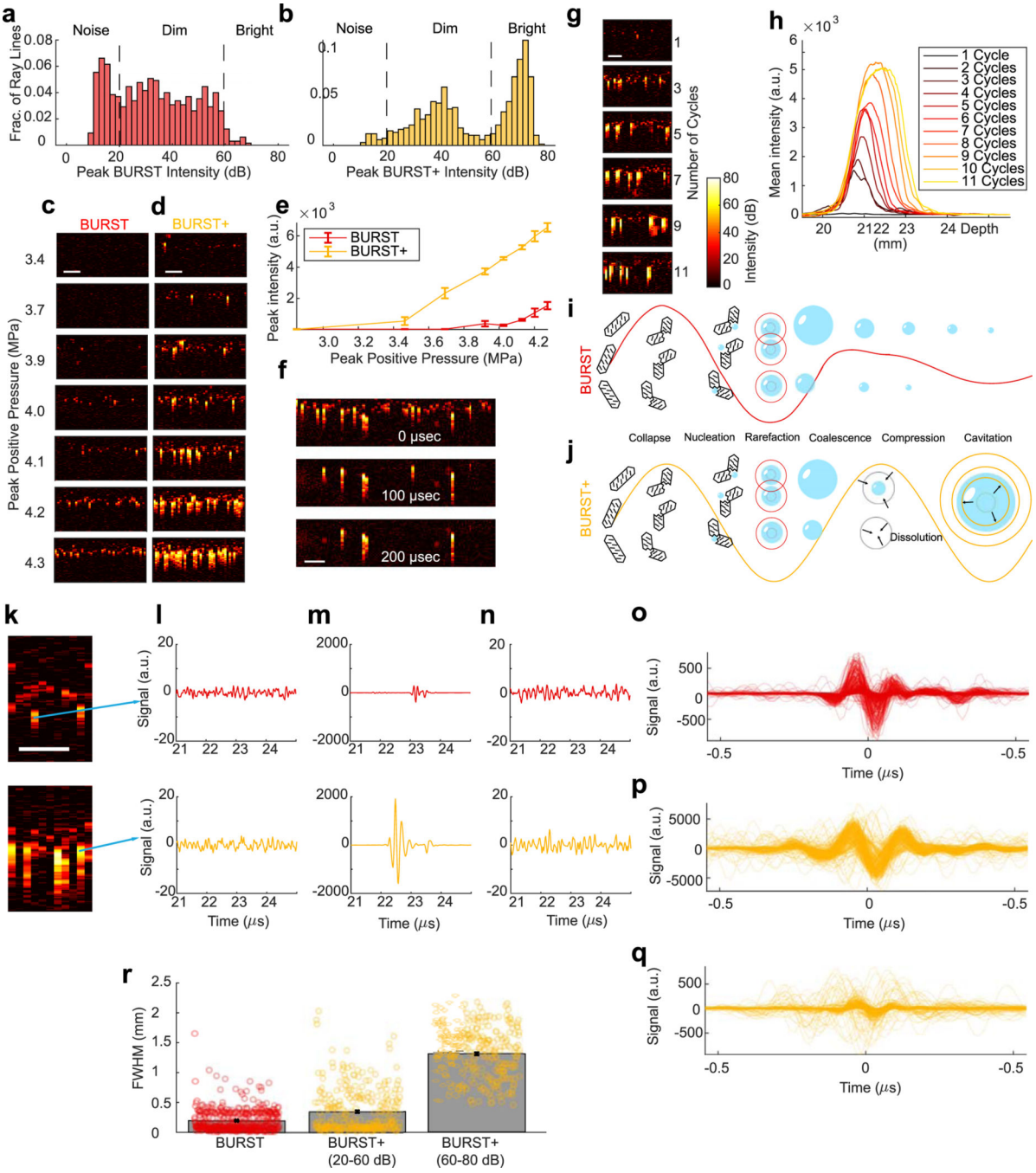

Extended Data Fig. 2. Collapse signal generation mechanism

The imaging target for all panels is ARG *E. coli* Nissle at 10^3 cells/ml in suspension. All images are displayed in dB scale with the same colormap shown in the bottom right of panel (g) (min: 0 dB, max: 80 dB). All scalebars are 2 mm. (**a**) Distribution of BURST ray line peak intensities (i.e. maxima over columns of pixels) for PPP = 4.3 MPa. N = 650. (**b**) Distribution of BURST+ ray line peak intensities for PPP = 4.3 MPa. N = 650. (**c**) BURST pressure ramp images with PPP ranging from 3.7 MPa to 4.3 MPa. (**d**) BURST+ pressure ramp with the same pressures as in (c). (**e**) Peak image intensity vs PPP for

BURST and BURST+. Error bars: SEM. N = 10 BURST acquisitions. (**f**) Image time series acquired with an ultrafast implementation of BURST+, with 1 frame/100 μsec, at 4.3 MPa. (**g**) Cycle ramp images with the number of transmit waveform cycles ranging from 0.5 cycles to 10.5 cycles and PPP held constant at 4.0 MPa. (**h**) Mean intensity of cycle ramp images vs. depth. Traces are averaged over 10 replicates. Error bars not shown for clarity. (**i**) Proposed mechanism to account for the presence of dim signals, but not bright signals, in BURST. (**j**) Proposed mechanism to account for the presence of both dim and bright sources in BURST+ and pulse sequences with more than one cycle. (**k**) BURST (top) and BURST+ (bottom) images at 4.3 MPa with arrows indicating the punctate signal whose RF data is plotted in the following panels. (**l-m**) Beamformed RF waveforms for the BURST (top) and BURST+ (bottom) ray lines in (k) indicated by the arrows. The waveforms are acquired from the pre-collapse, low-pressure frame (l), the first high-pressure frame (m), and the second high-pressure frame (n) of the BURST or BURST+ pulse sequence for arrival times corresponding to a depth range of 18 mm to 23 mm. (**o**) N = 464 RF waveforms corresponding to dim (20–60 dB) BURST signals aligned by peak envelope intensity. (**p**) N = 304 RF waveforms corresponding to bright (60–80 dB) BURST+ signals aligned by peak envelope intensity. (**q**) N = 308 RF waveforms corresponding to dim (20–60 dB) BURST+ signals aligned by peak envelope intensity. (**r**) Full width at half maximum (FWHM) for the envelopes of the RF waveforms shown in panels (o-q). N = 464 ray lines for BURST, N = 308 ray lines for dim (20–60 dB) BURST+, and N = 304 ray lines for bright (60–80 dB) BURST+. Error bars represent ± SEM.

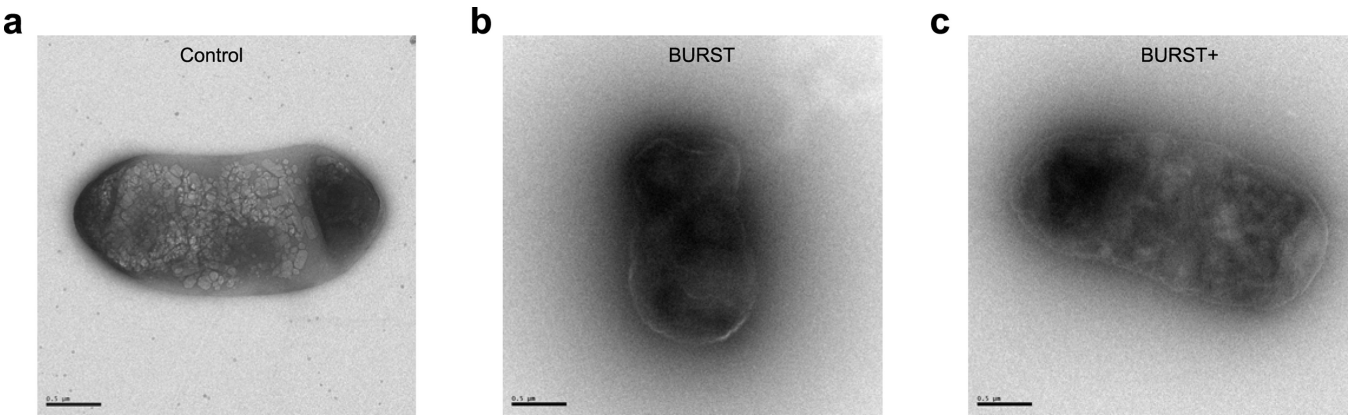

Extended Data Fig. 3. Transmission electron micrographs of ARG-expressing *E. coli* Nissle cells after imaging

(**a**) Representative cell from a sample not imaged with BURST or BURST+. A total of 14 micrographs of cells in this condition were acquired with similar results. (**b**) Representative cell from a sample imaged with BURST. A total of 13 micrographs of cells in this condition were acquired with similar results. (**c**) Representative cell from a sample imaged with BURST+. A total of 16 micrographs of cells in this condition were acquired with similar results. All scalebars: 500 nm. GVs are visible inside the control cell as lighter objects, and are absent in the imaged cells.

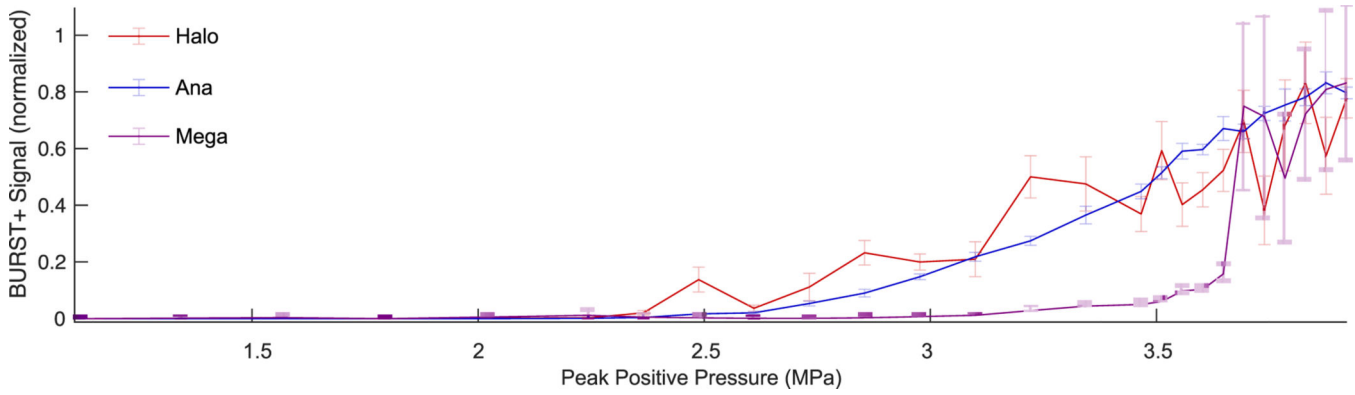

Extended Data Fig. 4. BURST thresholds for different types of gas vesicles

Normalized BURST+ signal as a function of peak positive pressure in BURST+ images of different types of GVs suspended in liquid buffer at concentrations of 10^{-5} OD_{500nm}. Halo GVs were purified from *Halobacterium salinarium*, Ana GVs were purified from *Anabaena flos-aquae*, and Mega GVs were purified from *E. coli*. N = 5 ray line acquisitions. Error bars represent ± SEM.

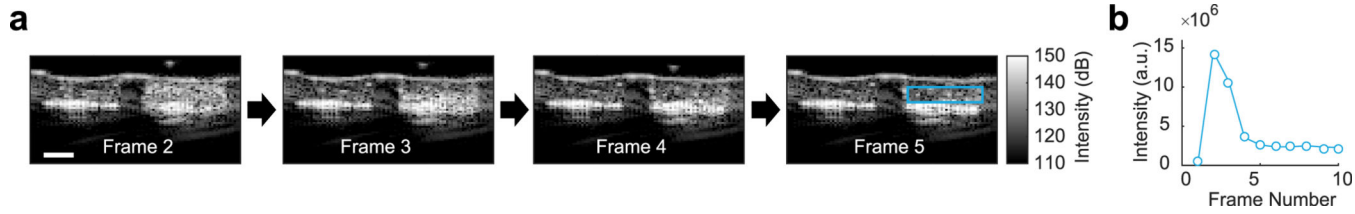

Extended Data Fig. 5. Acoustic shielding in BURST sequence at high ARG-expressing cell concentration

(**a**) Images from the high-pressure frames (frames 2–5) of a BURST+ sequence applied to a 1% agarose phantom with wells containing tissue-mimicking scatterers mixed with 10^8 cells/ml RFP-expressing *E. coli* Nissle (left) and ARG-expressing *E. coli* Nissle (right). Scale bars: 2 mm. (**b**) Mean pixel intensity vs. frame number for the ARG well, corresponding to the ROI of the same color in Frame 5 of the previous panel.

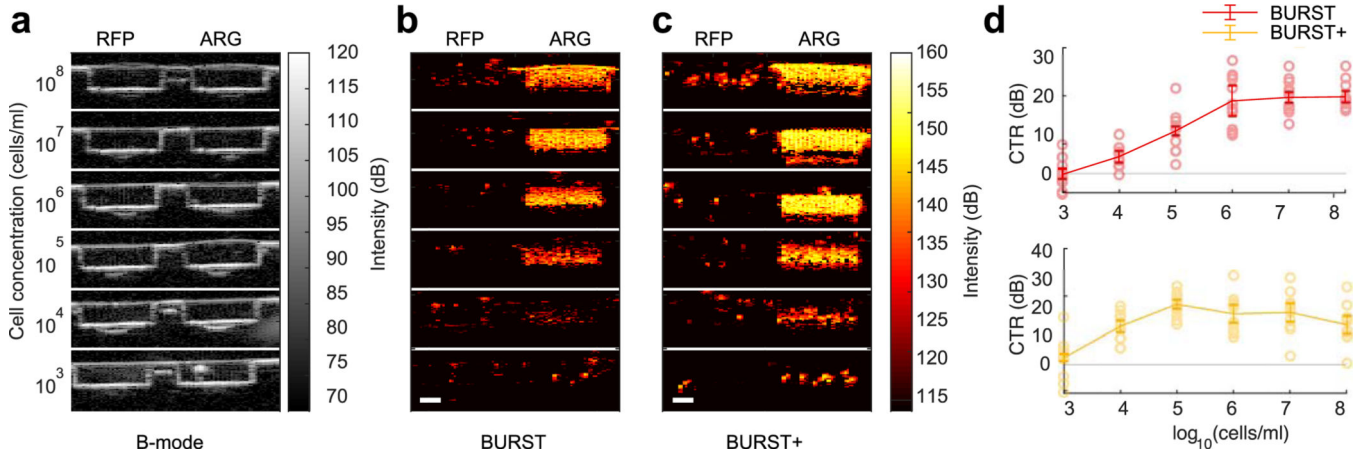

Extended Data Fig. 6. *In vitro* BURST imaging of ARG-expressing bacteria in plain agarose gel

(**a-c**) Array of ultrasound images of a cross section of rectangular wells containing Nissle *E. coli* embedded in 1% agarose wells within an agarose phantom. Each image contains a pair of wells, the left well containing RFP-expressing Nissle, the right well containing ARG-expressing Nissle. Rows correspond to cell concentrations, which range over six orders of magnitude. (**a**) B-mode images. (**b**) BURST images. (**c**) BURST+ images. The top edge of each image corresponds to a depth of 17.5 mm, the bottom to a depth of 23 mm. The left edge of each image corresponds to a lateral coordinate of −7 mm, the right to +7 mm. Scalebars: 2 mm. (**d**) Mean CTR vs log cell concentration for BURST and BURST+ on agarose-embedded cells. N = 12 wells, 4 from each of 3 biological replicates. CTR values represent the mean intensity of the ARG well relative to the mean intensity of the RFP well. Error bars: SEM.

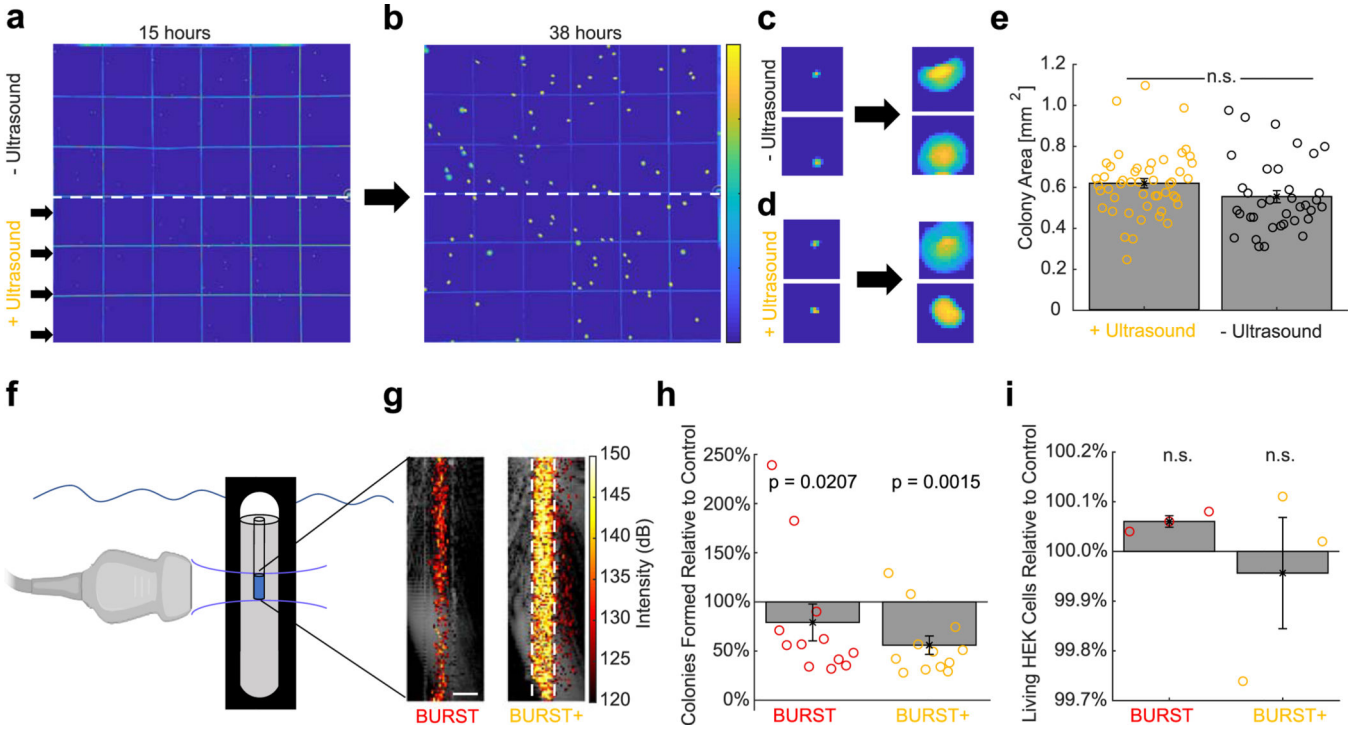

Extended Data Fig. 7. Effects of BURST imaging on cell viability

(**a**) Darkfield optical image of ARG-expressing *E. coli* Nissle colonies on an agar plate 15 h after seeding. Width of 1 square is 12.7 mm. To assay the effects of BURST and BURST+ imaging on bacterial population growth and confirm ARG re-expression after imaging, we cultured ARG Nissle as colonies embedded in soft hydrogel media and applied BURST+ to half the sample. (**b**) Image of the same plate 23 h after application of BURST+ to the bottom half. (**c**) Representative magnified images of colonies from the top half of the plate in (a) (left) and (b) (right). (**d**) Representative magnified images of colonies from the bottom half of the plate in (a) (left) and (b) (right). (**e**) Area of colonies exposed or not exposed to BURST+ at the 38-hour time point, 23 hours after application of BURST+. Error bars: SEM. N = 36 independent colonies in the –Ultrasound condition and N = 48 independent colonies in the +Ultrasound condition. Two-sided two-sample t-test. p = 0.10. (**f**) Illustration of the experimental setup for single-cell viability. An acoustic cuvette with mylar windows is filled

with 1% agarose and submerged in a water tank. A 2 mm diameter cylindrical inclusion in the agarose is filled with a suspension of GV-expressing cells (1×10^5 ARG Nissle cells/ml or 2.5×10^5 mARG HEK cells/ml) and imaged with BURST, BURST+, or 0.3 MPa B-mode as a control to assess the impact of BURST and BURST+ imaging on cells in liquid suspension. (**g**) Representative BURST and BURST+ images of ARG Nissle samples overlaid on a grayscale B-mode image. The edges of the cylindrical inclusion are indicated with dashed white lines. Scale bars: 2 mm. (**h**) Colony forming units of ARG-expressing *E. coli* Nissle cells for the samples exposed to BURST and BURST+ relative to B-mode controls. After imaging, the bacteria were plated on selective solid media and the number of colonies formed after 20 hours was counted. Error bars: SEM. N = 12 samples from 6 biological replicates. One-sided approximate permutation test with 10^7 permutations. p = 0.021 for BURST vs. control and p = 0.0015 for BURST+ vs. control. (**i**) Viable mARG-expressing HEK cells, as measured by flow cytometry, after exposure to BURST and BURST+, relative to B-mode controls. We exposed liquid suspensions of mARG-expressing HEK cells to these imaging modes in the same apparatus as described above for bacteria. Following ultrasound exposure, we counted the number of live (metabolically active) and dead cells using flow cytometry. We observed no significant difference in the viability of cells exposed to either BURST or BURST+ relative to the low-pressure controls. Error bars: SEM. N = 3 biological replicates. One-sided exact permutation test.p = 0.83 for BURST vs. control and p = 0.48 for BURST+ vs. control.

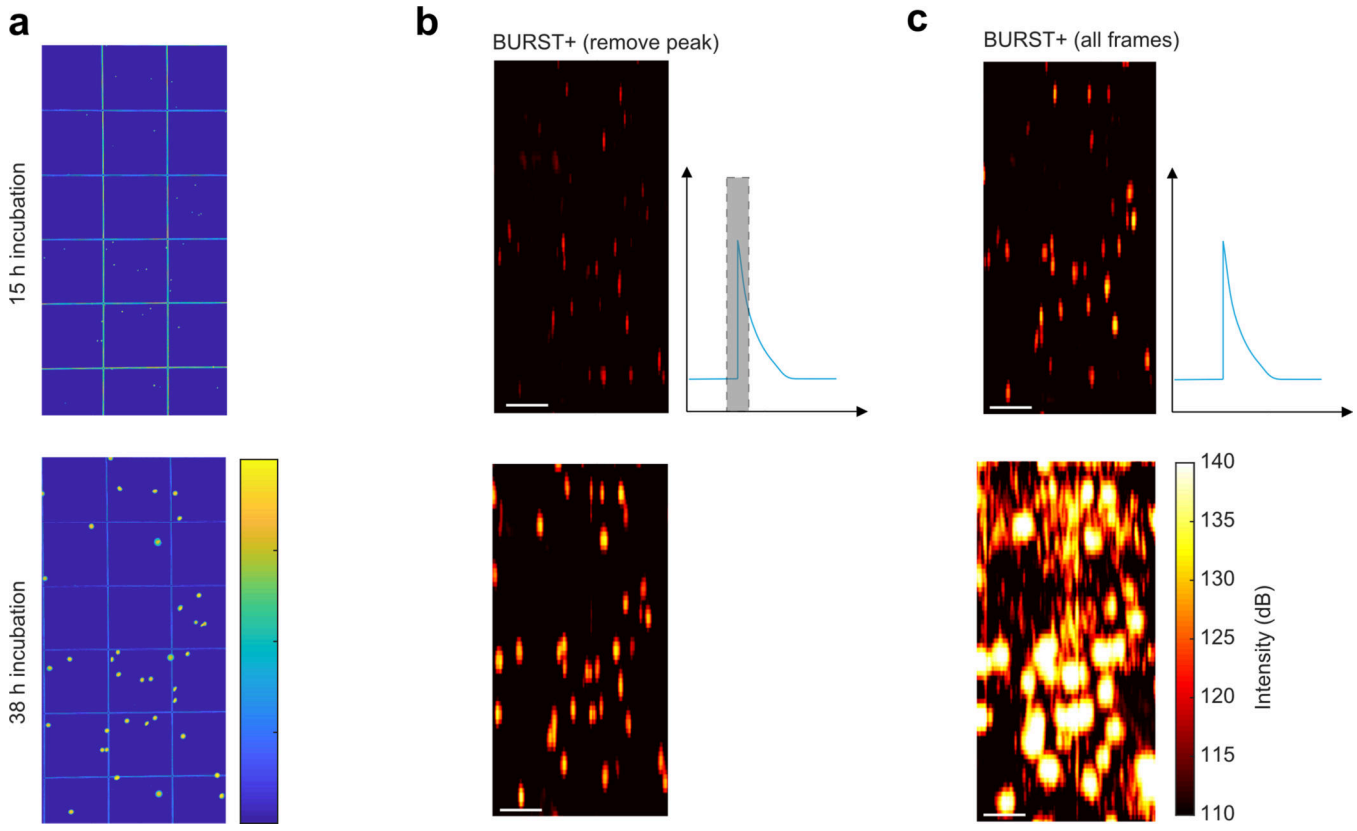

Extended Data Fig. 8. ARG-expressing Nissle colonies continue to grow and re-express GVs after exposure to BURST+

23 hours after initial exposure to BURST+, strong GV-specific BURST+ signal was observed from ARG-expressing Nissle colonies, confirming GV re-expression. Similar results were obtained with two additional plates. (**a**) Darkfield optical images of the half of the plate exposed to BURST+ after incubation at 30 °C for a total of 15 h (top) and 38 h (bottom). (**b**) BURST+ composite ultrasound images of the plate after 15 h (top) and 38 h (bottom), with the first collapse frame removed prior to template unmixing to reduce BURST signal area and allow comparison of signal spatial distribution with the optical image. The composite image was formed by taking the maximum of each BURST image plane along the axial dimension and concatenating the resulting rows of pixels to form 2D composite image. Prior to dB scaling, a 3×3 median filter was applied to the composite image, followed by a Gaussian filter with $\sigma = 1$. (**c**) The same BURST+ ultrasound images with all frames included in template unmixing. Scale bars: 10 mm.

Supplementary Material

Refer to Web version on PubMed Central for supplementary material.

Acknowledgments

We thank P. Dutka for assistance with electron microscopy, M. Swift for assistance with animal protocols, and B. Jin for the supine mouse illustration. DPS is supported by the NSF graduate research fellowship (award number 1745301). AB-Z is supported by the European Union's Horizon 2020 research and innovation programme under the Marie Skłodowska-Curie grant agreement No. 792866. AF was supported by the NSERC graduate fellowship. This research was funded by the National Institutes of Health (grant R01-EB018975 to MGS). Related research in the Shapiro laboratory is also supported by the Chan-Zuckerberg Initiative, Heritage Medical Research Institute, Burroughs Wellcome Career Award at the Scientific Interface, the Pew Scholarship in the Biomedical Sciences and the Packard Fellowship for Science and Engineering.

References

1. Tsien RYThe Green Fluorescent Protein. Annual Review of Biochemistry67, 509–544 (1998).
2. Ntziachristos V. Going deeper than microscopy: the optical imaging frontier in biology. Nature Methods7, 603–614 (2010). [PubMed: 20676081]
3. Piraner DIet al.Going Deeper: Biomolecular Tools for Acoustic and Magnetic Imaging and Control of Cellular Function. Biochemistry56, 5202–5209 (2017). [PubMed: 28782927]
4. Maresca D. et al.Biomolecular Ultrasound and Sonogenetics. Annu. Rev. Chem. Biomol. Eng. (2018) doi:10.1146/annurev-chembioeng-060817-084034.
5. Shapiro MGet al.Biogenic gas nanostructures as ultrasonic molecular reporters. Nature Nanotechnology9, 311–316 (2014).
6. Bourdeau RWet al.Acoustic reporter genes for noninvasive imaging of microorganisms in mammalian hosts. Nature553, 86–90 (2018). [PubMed: 29300010]
7. Farhadi A, Ho GH, Sawyer DP, Bourdeau RW & Shapiro MG Ultrasound imaging of gene expression in mammalian cells. Science 365, 1469–1475 (2019). [PubMed: 31604277]
8. Round JL & Mazmanian SK The gut microbiota shapes intestinal immune responses during health and disease. Nature Reviews Immunology 9, 313–323 (2009).
9. Derrien M. & van Hylckama Vlieg JET Fate, activity, and impact of ingested bacteria within the human gut microbiota. Trends in Microbiology 23, 354–366 (2015). [PubMed: 25840765]
10. Simon GL & Gorbach SL Intestinal flora in health and disease. Gastroenterology 86, 174–193 (1984). [PubMed: 6357937]
11. Savage DCMicrobial ecology of the gastrointestinal tract. Annual review of microbiology31, 107–133 (1977).

12. Donaldson GP, Lee SM & Mazmanian SK Gut biogeography of the bacterial microbiota. Nature Reviews Microbiology 14, 20–32 (2016). [PubMed: 26499895]
13. Riglar DT & Silver PA Engineering bacteria for diagnostic and therapeutic applications. Nature Reviews Microbiology 16, 214–225 (2018). [PubMed: 29398705]
14. Maresca D. et al.Nonlinear ultrasound imaging of nanoscale acoustic biomolecules. Appl. Phys. Lett. 110, 073704 (2017).
15. Maresca D, Sawyer DP, Renaud G, Lee-Gosselin A. & Shapiro MG Nonlinear X-Wave Ultrasound Imaging of Acoustic Biomolecules. Phys. Rev. X 8, 041002 (2018).
16. Walsby AEGas vesicles. Microbiology and Molecular Biology Reviews58, 94–144 (1994).
17. Pfeifer F. Haloarchaea and the Formation of Gas Vesicles. Life5, 385–402 (2015). [PubMed: 25648404]
18. Bar-Zion A. et al.Acoustically Detonated Biomolecules for Genetically Encodable Inertial Cavitation. bioRxiv 620567 (2019).
19. Demené C. et al.Spatiotemporal Clutter Filtering of Ultrafast Ultrasound Data Highly Increases Doppler and fUltrasound Sensitivity. IEEE Transactions on Medical Imaging34, 2271–2285 (2015). [PubMed: 25955583]
20. Sheeran PS & Dayton PA Phase-change contrast agents for imaging and therapy. Curr. Pharm. Des. 18, 2152–2165 (2012). [PubMed: 22352770]
21. Stiel ACet al.High-contrast imaging of reversibly switchable fluorescent proteins via temporally unmixed multispectral optoacoustic tomography. Opt. Lett., OL40, 367–370 (2015).
22. Yao J. et al.Multiscale photoacoustic tomography using reversibly switchable bacterial phytochrome as a near-infrared photochromic probe. Nature Methods13, 67–73 (2016). [PubMed: 26550774]
23. Patterson G, Davidson M, Manley S. & Lippincott-Schwartz J. Superresolution Imaging using Single-Molecule Localization. Annual Review of Physical Chemistry 61, 345–367 (2010).
24. Frinking PJA, Cespedes EI, Kirkhorn J, Torp HG & Jong N. de. A new ultrasound contrast imaging approach based on the combination of multiple imaging pulses and a separate release burst. IEEE Transactions on Ultrasonics, Ferroelectrics, and Frequency Control 48, 643–651 (2001).
25. Meng Z. et al.Ultrasound-Responsive Conversion of Microbubbles to Nanoparticles to Enable Background-Free in Vivo Photoacoustic Imaging. Nano Lett. 19, 8109–8117 (2019). [PubMed: 31597418]
26. Huynh E. et al.In situ conversion of porphyrin microbubbles to nanoparticles for multimodality imaging. Nature Nanotechnology10, 325–332 (2015).
27. Yoon YIet al.Ultrasound-Mediated Gene and Drug Delivery Using a Microbubble-Liposome Particle System. Theranostics4, 1133–1144 (2014). [PubMed: 25250094]
28. Ramnarine KV, Anderson T. & Hoskins PR Construction and geometric stability of physiological flow rate wall-less stenosis phantoms. Ultrasound in medicine & biology 27, 245–250 (2001). [PubMed: 11316533]
29. Hynynen K. The threshold for thermally significant cavitation in dog's thigh muscle in vivo. Ultrasound in Medicine &Biology17, 157–169 (1991).
30. Zhang Y. et al.Non-invasive multimodal functional imaging of the intestine with frozen micellar naphthalocyanines. Nature Nanotechnology9, 631–638 (2014).
31. Sheppard M. et al.Dynamics of bacterial growth and distribution within the liver during Salmonella infection. Cellular Microbiology5, 593–600 (2003). [PubMed: 12925129]
32. Prindle A. et al.Genetic circuits in Salmonella typhimurium. ACS synthetic biology1, 458–464 (2012). [PubMed: 23097749]
33. Kaliss N. & Pressman D. Plasma and Blood Volumes of Mouse Organs, As Determined with Radioactive Iodoproteins. Proceedings of the Society for Experimental Biology and Medicine 75, 16–20 (1950). [PubMed: 14797719]
34. . Fink MP Animal models of sepsis. Virulence 5, 143–153 (2014). [PubMed: 24022070]
35. Lakshmanan A. et al.Molecular Engineering of Acoustic Protein Nanostructures. ACS Nano10, 7314–7322 (2016). [PubMed: 27351374]

36. Maresca D. et al.Acoustic biomolecules enhance hemodynamic functional ultrasound imaging of neural activity. NeuroImage209, 116467 (2020). [PubMed: 31846757]

37. Lu GJ, Farhadi A, Mukherjee A. & Shapiro MG Proteins, air and water: reporter genes for ultrasound and magnetic resonance imaging. Current Opinion in Chemical Biology 45, 57–63 (2018). [PubMed: 29549770]

38. Lippincott-Schwartz J. & Patterson GH Development and Use of Fluorescent Protein Markers in Living Cells. Science 300, 87–91 (2003). [PubMed: 12677058]

39. Betzig E. et al.Imaging Intracellular Fluorescent Proteins at Nanometer Resolution. Science313, 1642–1645 (2006). [PubMed: 16902090]

40. Rust MJ, Bates M. & Zhuang X. Sub-diffraction-limit imaging by stochastic optical reconstruction microscopy (STORM). Nat Methods 3, 793–796 (2006). [PubMed: 16896339]

41. Keller PJ, Schmidt AD, Wittbrodt J. & Stelzer EHK Reconstruction of Zebrafish Early Embryonic Development by Scanned Light Sheet Microscopy. Science 322, 1065–1069 (2008). [PubMed: 18845710]

42. . Danino T, Lo J, Prindle A, Hasty J. & Bhatia SN In Vivo Gene Expression Dynamics of Tumor-Targeted Bacteria. ACS Synth. Biol. 1, 465–470 (2012). [PubMed: 23097750]

43. Lakshmanan A. et al.Preparation of biogenic gas vesicle nanostructures for use as contrast agents for ultrasound and MRI. Nature Protocols12, 2050–2080 (2017). [PubMed: 28880278]

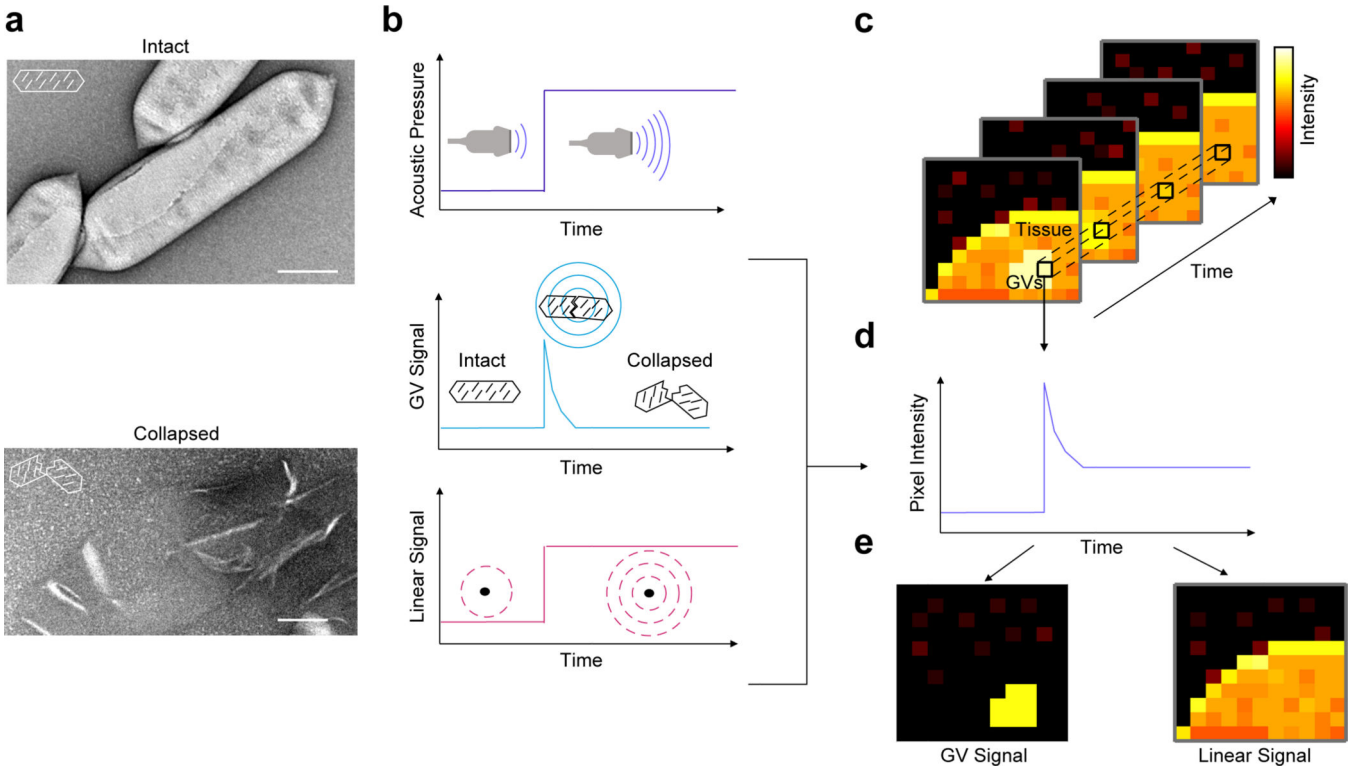

Figure 1 |. BURST paradigm.

(**a**) TEM images of intact (top) and collapsed (bottom) GVs from *Anabaena flos-aquae*. Scale bars: 100 nm. Image representative of >5 fields of view. (**b**) Illustration of the BURST pulse sequence, showing the step change in applied acoustic pressure (top), the resulting transient increase in GV signal (middle) and the persistent increase in linear scatterer signal (bottom). (**c**) Illustration of an image time series generated by the high-pressure segment of the BURST sequence applied to a hypothetical target, which consists of scattering tissue with ARG-expressing cells located at the center. (**d**) Illustration of intensity time course for a pixel location in the region containing GVs. (**e**) Illustration of the result of the signal template unmixing algorithm applied to the image timeseries, generating separate images representing the contribution of GV signal (left) and linear signal (right) to the recorded image timeseries.

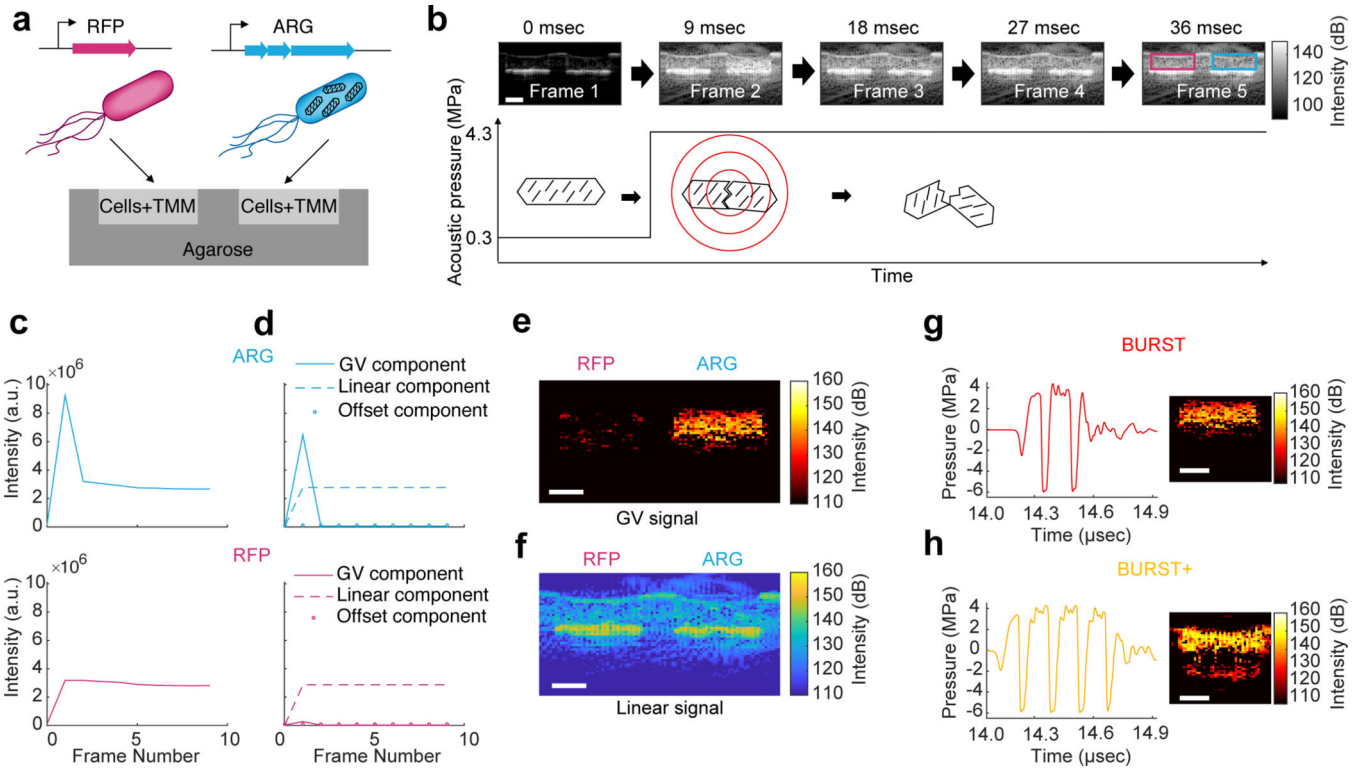

Figure 2 |. BURST imaging of ARG-expressing cells.

(**a**) Illustration of the agarose gel phantom containing cells engineered to express RFP or ARG, mixed with tissue-mimicking material (TMM). (**b**) Representative images from frames 1–5 of a BURST sequence applied to a 1% agarose phantom with wells containing TMM mixed with 10^7 cells/ml RFP-expressing (left) or ARG-expressing *E. coli* Nissle cells (right). The acoustic pressure is ramped from 0.27 MPa in the first frame to 4.3 MPa for the remaining 4 frames, as shown in the illustrated plot below the images. Scale bars: 2 mm. (**c**) Mean pixel intensity vs. frame number in ROIs containing RFP or ARG-expressing cells, outlined in (b). (**d**) Decomposition of the time traces in (c) using the template unmixing algorithm. (**e**) Output of the template unmixing algorithm applied pixel-wise to the full field of view, showing the estimated contribution of GV signal to every pixel. (**f**) Estimated contribution of linear tissue signal to every pixel. (**g**) Fiberoptic hydrophone measurement of the acoustic waveform used in the BURST high-pressure transmit, and the resulting BURST image of a phantom identical to the one described in (a). (**h**) Acoustic waveform for BURST+ and the corresponding image. The measured output of the transducer is slightly extended due to ringdown. The number of cycles was set to 3 to enable nanobubble cavitation while preserving axial resolution. All scale bars: 2 mm.

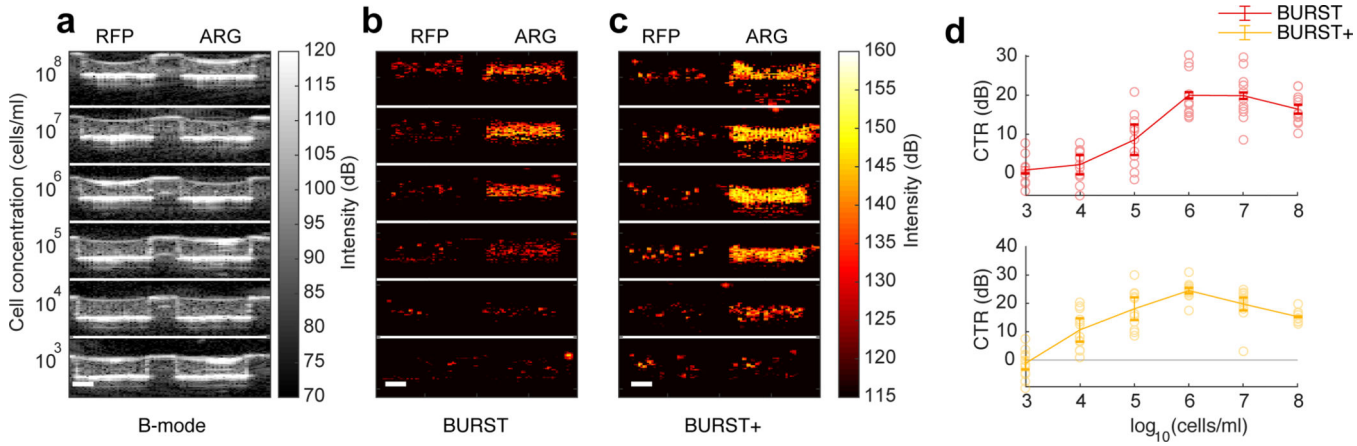

Figure 3 |. Detection sensitivity of BURST imaging.

(**a-c**) Ultrasound images of rectangular wells containing *E. coli* Nissle cells embedded with tissue-mimicking material (TMM) in an agarose phantom. The left well contains cells expressing RFP, and the right well contains cells expressing ARG. Rows correspond to cell concentrations ranging over six orders of magnitude. (**a**) B-mode images. (**b**) BURST images. (**c**) BURST+ images. The top edge of each image corresponds to a depth of 17.5 mm, the bottom to a depth of 23 mm. Scalebars: 2 mm. (**d**) Mean contrast-to-tissue ratio (CTR) vs log cell concentration for BURST and BURST+ on TMM-embedded cells. N = 12 wells (4 from each of 3 biological replicates). CTR represents the mean intensity of the ARG well relative to the mean intensity of the RFP well. Error bars represent SEM.

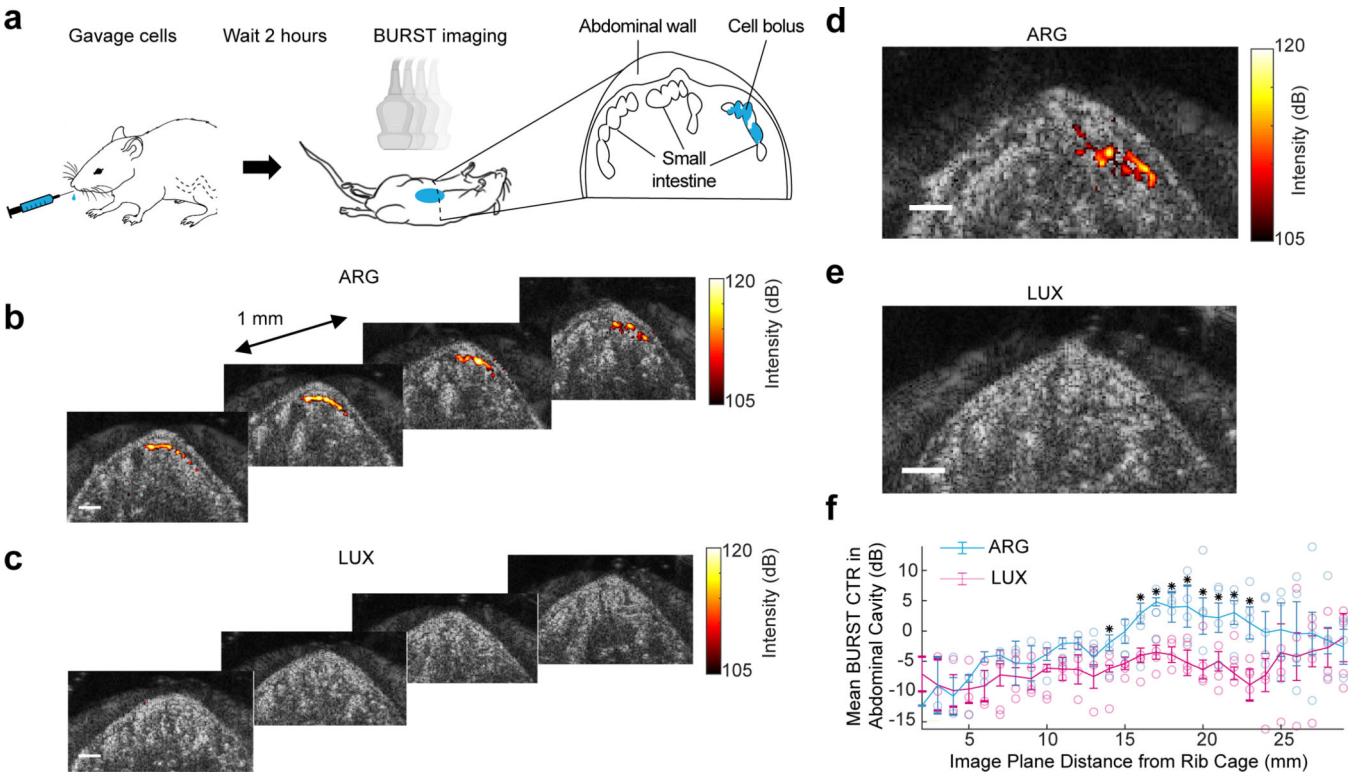

Figure 4 |. BURST imaging of orally gavaged cells.

(**a**) Illustration of the oral gavage experiment and the expected distribution of ARG-expressing cells as viewed in a cross section of the mouse abdomen. (**b-c**) Coronal BURST images (heat colormap) of the abdomen overlaid on the corresponding anatomical B-mode images (grayscale), acquired 2 hours after oral gavage of 2×10^8 ARG-expressing (**b**) or LUX-expressing (**c**) *S. typhimurium* cells. The four images correspond to coronal planes 18 mm to 21 mm caudal to the rib cage. The patches of supra-threshold BURST signal have dimensions of approximately 2 mm × 1 mm, are located 1 mm below the abdominal wall, and span several contiguous frames in the abdomen. Scale bars: 2 mm. (**d-e**) Magnified images of coronal planes directly preceding those in (b-c) (17 mm). Scale bars, 2 mm. This experiment was repeated independently with four mice for both the LUX control and ARG conditions. In all four mice in the control condition, no supra-threshold BURST signal was observed inside the abdominal cavity at any plane, similar to the LUX gavage images in (c) and (e). In three of the mice in the ARG condition, between seven and ten planes contained patches of supra-threshold BURST signal similar to the images in (b) and (d). (**f**) BURST CTR as a function of image plane location in mice gavaged with ARG-expressing or LUX-expressing cells. The CTR is calculated based on the mean intensity of ROIs manually drawn to encompass the ventral half of the abdominal cavity. Tissue ROIs encompassed a rectangular region in the dorsal half of the abdominal cavity. Error bars represent SEM. N = 4 mice. Asterisks indicate $p < 0.05$. One-sided exact permutation test. The exact p-values for each plane are as follows, where the variable x represents distance from the rib cage in mm: [(x=1, p=1.00), (x=2, p=0.67), (x=3, p=0.70), (x=4, p=0.30), (x=5, p=0.13), (x=6,p=0.20), (x=7, p=0.27), (x=8, p=0.27, (x=9, p=0.06), (x=10, p=0.06), (x=11, p=0.09), (x=12, p=0.14), (x=13, p=0.01), (x=14, p=0.06), (x=15, p=0.03), (x=16, p=0.01), (x=17, p=0.03), (x=18,

p=0.03), (x=19, p=0.03), (x=20, p=0.03), (x=21, p=0.01), (x=22, p=0.03), (x=23, p=0.11), (x=24, p=0.29), (x=25, p=0.31), (x=26, p=0.24, (x=27, p=0.46), (x=28, p=0.63)].

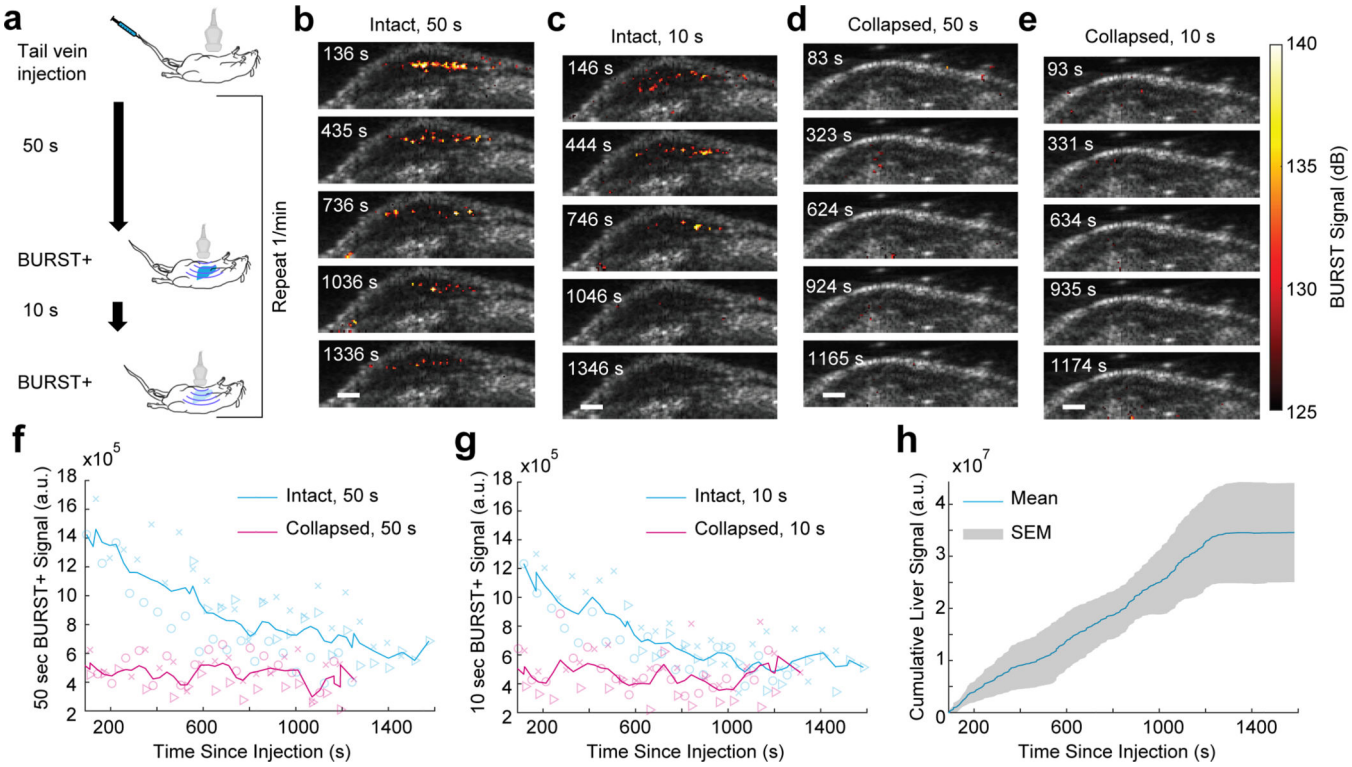

Figure 5 |. Dynamic BURST imaging of systemically injected probiotics.

(**a**) Illustration of the experiment. (**b-e**) Representative coronal BURST+ images (heat colormap) of the liver overlaid on the corresponding anatomical B-mode images (grayscale), acquired at the indicated time points following tail vein injection of 50 μl of ARG-expressing *S. typhimurium* at 3×10^5 cells/ml. Each minute following an initial BURST+ acquisition, images were acquired after waiting 50 s (b) and then after waiting 10 s (c). As a control, the same experiment was performed with cells whose GVs were hydrostatically pre-collapsed prior to injection (d-e). Scalebars: 2 mm. (**f-g**) Mean BURST+ signal in the liver as a function of time since injection for images acquired 50 s (f) or 10 s (g) after the previous image. Markers with different shapes indicate data points from different animals. (**h**) Estimated cumulative signal due to cells cleared from the bloodstream and accumulated in the liver ± SEM. N = 3 mice per condition.

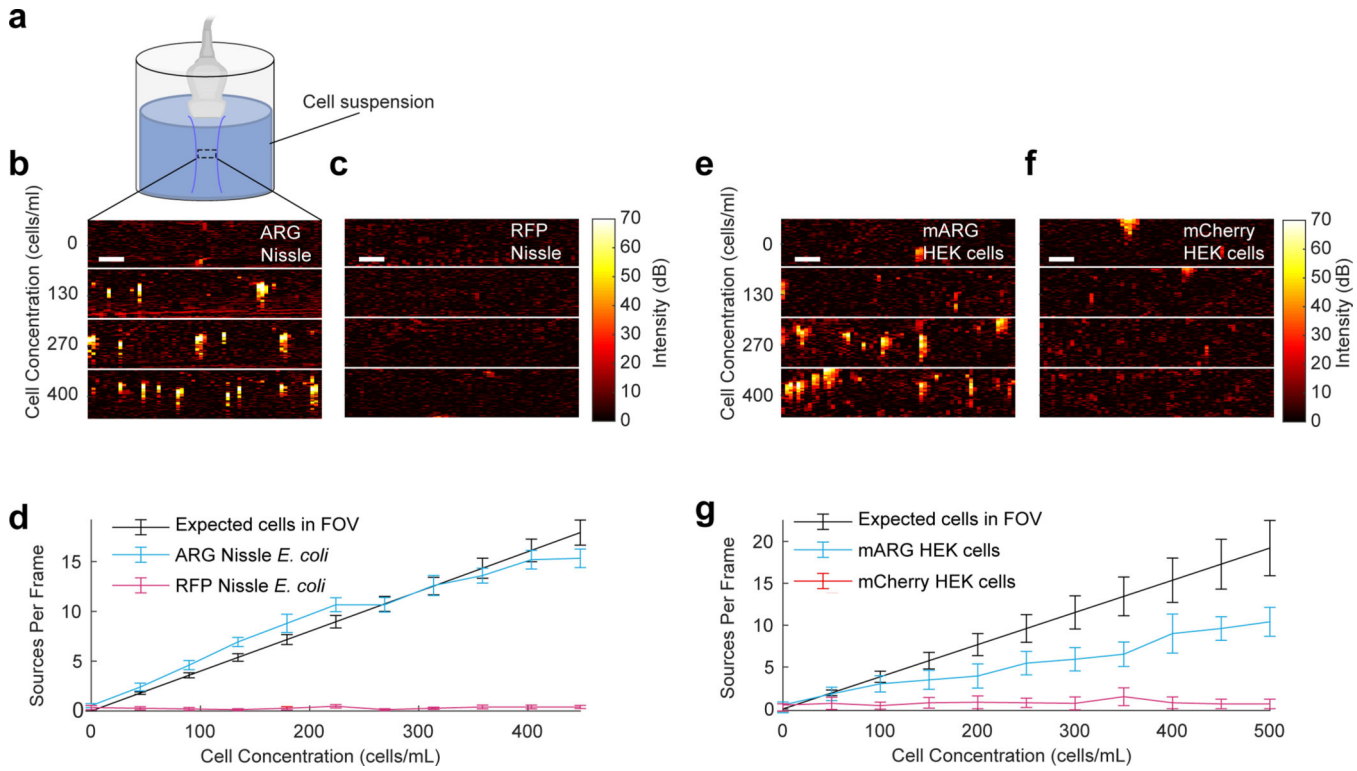

Figure 6 |. Single cell imaging using BURST.

(**a**) Illustration of the experimental setup, in which bacterial or mammalian cells are suspended in liquid at dilute concentrations while being imaged in the focal zone of the transducer. (**b**) Representative BURST+ images showing single sources in liquid buffer suspension of ARG-expressing *E. coli* Nissle cells at the indicated concentrations. (**c**) Representative BURST+ images of RFP-expressing *E. coli* Nissle cells. (**d**) Average number of single sources counted in images acquired with BURST+ vs. cell concentration for ARG- and RFP-expressing *E. coli* Nissle cells. To quantify the number of signal sources in our field of view, all contiguous signals distinct from background noise were counted, regardless of their size. Error bars represent SEM. N = 3 biological replicates. Mean counts from 5 frames were used for each biological replicate. An independent estimate of the expected number of cells in the transducer's field of view, based on cell counting by fluorescence microscopy, is also plotted for comparison. (**e**) Representative BURST+ images of suspended mARG-expressing HEK cells at the indicated concentrations. Cell concentrations were measured with optical cytometry. (**f**) Representative BURST+ images of mCherry-expressing HEK cells. (**g**) Average number of single sources counted in images acquired with BURST+ vs. cell concentration for mARG and mCherry-expressing HEK cells. Error bars represent SEM for N = 4 biological replicates. Mean counts from 5 frames were used for each biological replicate.